https://doi.org/10.1016/j.energy.2017.09.036

Performance improvement of a direct carbon solid oxide fuel cell system by combining with a Stirling cycle

Haoran Xu[1,2], Bin Chen[2], Peng Tan[2], Houcheng Zhang[1,2,*], Jinliang Yuan[3], Jiang Liu[4], Meng Ni[2,*]

[1]*Department of Microelectronic Science and Engineering, Ningbo University, Ningbo 315211, China*

[2]*Building Energy Research Group, Department of Building and Real Estate, The Hong Kong Polytechnic University, Hung Hom, Kowloon, Hong Kong, China*

[3]*Faculty of Maritime and Transportation, Ningbo University, Ningbo 315211, China*

[4]*New Energy Research Institute, School of Environment and Energy, South China University of Technology, Guangzhou 510006, China*

Abstract: An external heat source and a Stirling cycle are proposed for performance improvement of a direct carbon solid oxide fuel cell (DC-SOFC) system. The amount of the heat released in the DC-SOFC is determined based on a previously validated 2D tubular DC-SOFC model, in which the electrochemical reaction, chemical reactions, ion/electronic charge transport, mass transport and momentum transport are fully considered. Numerical calculations show that the overall heat released in the cell may be smaller than, equal to or larger than the heat required by the internal Boudouard reaction, and accordingly, three different operating modes of the system are given. The analytical expressions for the equivalent power output and efficiency for the DC-SOFC, Stirling cycle and the hybrid system are specified under different operating conditions. The results show that the power density and efficiency of the proposed system allow 4000 W m^{-2} and 30% larger than that of the stand-alone DC-SOFC at 30000 A m^{-2}, respectively. Parametric studies also show that a higher operating temperature and a smaller distance between carbon layer and anode will increase the overall power density and efficiency of the proposed system.

Keywords: Solid oxide fuel cell; Solid carbon; Boudouard reaction; Stirling cycle; heat management

*Corresponding authors.
Email addresses: zhanghoucheng@nbu.edu.cn (H. Zhang), bsmengni@polyu.edu.hk (M. Ni).

1. Introduction

Despite the tendency in reducing reliance on fossil fuels as energy resources due to environmental problems, coal remains to be a main resource due to its wide availability and low price. Solid carbon like coal is usually directly burned in traditional thermal power plants for electricity generation in an inefficient way with emission of hazardous gases. Thus, there is an urgent need to develop new methods for coal utilization. Direct carbon fuel cells (DCFCs) are promising electrochemical devices that enable to directly convert the chemical energy of solid carbon into electricity with high efficiency and low emissions [1-7].

DC-SOFCs operate on the same electrochemical principles as conventional solid oxide fuel cells (SOFCs) but use solid carbon as fuel [8, 9]. As the solid carbon particles are larger than the pores of SOFC anode, they cannot reach the triple phase boundary (TPB) of anode. It is well accepted that the operation of DC-SOFC is based on the "CO_2 shuttling theory": the solid carbon is gasified by CO_2 to produce CO, which subsequently participates in the electrochemical reactions for electricity power generation. The dense oxygen-ion-conducting electrolyte and high-temperature operation characteristic of DC-SOFC provide the possibility to easily handle the exhaust gas emission control and use the low cost catalyst such as Ni [10, 11].

Based on the "CO_2 shuttling theory", extensive experimental and modeling works have been conducted to further improve the DC-SOFC performance [12]. In a study conducted by Lee et al. [13], a thermodynamic model was developed to analyze the efficiency of DC-SOFC, which was considerably higher than that of the traditional thermal power plants. The

performance of DC-SOFC is limited by the carbon gasification kinetics as the kinetics of chemical reactions is usually much slower than that of electrochemical reactions [14-17]. To improve the DC-SOFC performance, various catalysts for carbon gasification have been developed [18-20]. In a recent study, a power density of 434 mW cm^{-2} at 1123 K has been achieved, which is only slightly smaller than that with H_2 fuel (480 mW cm^{-2}) [17]. As CO is generated in the anode chamber, CO and electricity co-generation in DC-SOFCs was proposed by Xie et al [21] and an overall efficiency of 76.5% was achieved with CO and electricity as energy output. Mathematical modeling studies were conducted to understand the physical/chemical processes in DC-SOFC for CO and electricity cogeneration [22, 23]. It was found that the heat generation from the irreversible losses in DC-SOFC is sufficient to sustain the required temperature of the cell at a large operating current density, while an external heating is needed at a high operating potential. Therefore, the efficiency of DC-SOFCs could be further improved if the excess waste heat is utilized at a larger operating current density.

Obviously, the high-quality waste heat generated in DC-SOFC can be recovered for combined heat and power (CHP) generation. Based on various analysis approaches [24-26], extensive studies have been conducted on SOFC-based hybrid systems fueled with diverse fuels [27, 28] for different applications [29, 30]. A number of thermodynamic devices have been employed to utilize the waste heat from SOFCs including heat engines [31-33], gas turbines [34, 35], and thermoelectric generators [36], etc. Among various bottoming thermal devices, Stirling cycle engines are referred as the external combustion heat engines, which are based on a regenerative closed power cycle named Stirling cycle[37]. Stirling cycle engines

enable efficient conversion of waste heat into mechanical work, which have drawn much attention recently because of their low emission, low vibration, high reliability and low maintenance cost [38-40]. Although a few studies have been conducted to recover the waste heat from SOFC through Stirling cycle [41-43], the study on the heat management of DC-SOFC is still lacking.

In this work, a previously developed 2D tubular DC-SOFC model is adopted to study the DC-SOFC system integrated with an external heat source and a Stirling cycle for heat management. Based on the modeling analysis, different operating modes of this new system are specified under different operating conditions. The performance of the proposed system is evaluated based on the power output and efficiency mathematical expressions. The advantages of the new system layout are shown by numerical predictions. Finally, the effects of some design parameters and the operating conditions on the performance of the system are discussed.

2. System description

The proposed hybrid system consists of a DC-SOFC, an external heat source, a Stirling cycle engine and a regenerator, as shown in Fig. 1. The DC-SOFC electrochemically converts the chemical energy of solid carbon into electrical power P_{SOFC}. To ensure the normal operation of the DC-SOFC, an amount of heat Q (J S^{-1}) should be provided to or extracted from the DC-SOFC. When the DC-SOFC is operated in the endothermic mode, the external heat source should be connected. When the DC-SOFC is operated in the exothermic mode, the

Stirling cycle should be connected to produce additional power P_{SHE}. The regenerator preheats the inlet reactants with the help of the heat contained in the outlet high-temperature products.

For simplification, the following assumptions are adopted [23, 44]:

- The distribution of electrochemical reaction sites is uniform in the porous electrodes. Electronic- and ionic-conducting materials are continuous and homogeneous;
- Ionic and electronic charge transport processes take place in the Positive Electrode-Electrolyte-Negative electrode assembly, and the charge transfer reaction can take place at TPB throughout the porous electrode;
- All gases involved in the DC-SOFC are ideal gases and the gas flows are incompressible;
- Operating temperature of the DC-SOFC is uniform and constant;
- Volume and shape of solid carbon fuel do not change with time;
- Working substance inside the Stirling cycle is ideal gas;
- Heat transfers between the Stirling cycle and the DC-SOFC and the environment obey Newton's law.

2.1 DC-SOFC

The schematic of the electrolyte-supported tubular DC-SOFC is shown in Fig. 2. Solid carbon and air are supplied to the anode and cathode channels, respectively. CO molecules are produced through Boudouard reaction in anode chamber and then diffuse into the porous electrode, where they react with O^{2-} ions at the TPB sites to generate electricity and form CO_2 molecules. The generated CO_2 molecules subsequently diffuse back from TPB to the anode

chamber to continue the Boudouard reaction for CO molecules generation. These processes repeat between the carbon layer and the porous electrode to generate electricity.

The well-developed 2D DC-SOFC model consisting of chemical reaction, electrochemical reaction, mass transport, momentum transport and heat transfer sub-models is adopted to describe the chemical reaction, electrochemical reaction, ionic/electronic charge transport, mass transport, momentum transport and heat transfer [23]. The model has been validated in the previously study [23], in which it showed good agreement between the simulation results and the experimental data [17]. In the following, each sub-model will be briefly introduced.

2.2.1 Chemical reaction model

The key chemical reaction in DC-SOFC is the Boudouard reaction (Eq. (1)), which converts solid carbon into CO by consuming CO_2. Its reaction rate can be calculated as Eq. (2) [39].

$$\mathrm{C} + \mathrm{CO_2} = 2\mathrm{CO} \tag{1}$$

$$R_{rb} = k_{rb}\exp(-E_{rb}/RT)c_{CO_2} \tag{2}$$

2.2.2 Electrochemical reaction model

CO gas produced from Boudouard reaction will transport to anode TPB sites where it reacts electrochemically with O^{2-} and release electrons as shown in Eq. (3). The O^{2-} ion is reduced in cathode and transported through the electrolyte as shown in Eq. (4).

$$\mathrm{CO} + \mathrm{O^{2-}} \rightarrow \mathrm{CO_2} + 2\mathrm{e^-} \tag{3}$$

$$\mathrm{O_2} + 4\mathrm{e^-} \rightarrow 2\mathrm{O^{2-}} \tag{4}$$

The related equilibrium potential (E_{CO}) for above equations can be calculated as Eq. (5),

$$E_{CO} = E_{CO}^{0} + \frac{RT}{2F}\ln\left[\frac{P_{CO}^{L}(P_{O_2}^{L})^{1/2}}{P_{CO_2}^{L}}\right] \tag{5}$$

where R and F are the universal gas constant (8.3145 J mol^{-1} K^{-1}) and Faraday's constant (96485 C mol^{-1}), respectively. T is cell temperature (K) and P^L is local gas partial pressure (Pa). E_{CO}^0 is the standard potential (V), which can be calculated by Eq. (6) [40]

$$E_{CO}^0 = 1.46713 - 0.0004527T \text{ (V)} \quad (6)$$

As local gas partial pressure is used in the calculation, only activation overpotential loss (η_{act}) and ohmic overpotential losses (η_{ohmic}) are considered for the calculation of the operating potential (E) as shown in Eq. (7):

$$E = E_{CO}^0 - \eta_{act} - \eta_{ohmic} \quad (7)$$

The relationship between current density and these two overpotentials are described by Butler-Volmer equation (Eq. (8)) and Ohm's law (Eq. (9)), respectively [41].

$$i = i_0 \left\{ \exp\left(\frac{\alpha n F \eta_{act}}{RT}\right) - \exp\left(\frac{(1-\alpha) n F \eta_{act}}{RT}\right) \right\} \quad (8)$$

$$i = -\sigma^{eff} \nabla(\phi) \quad (9)$$

where i and i_0 are operating current density (A m^{-2}) and exchange current density (A m^{-2}), respectively. α is the electron transfer coefficient, n is the number of transferred electrons per electrochemical reaction, σ^{eff} and ϕ are effective conductivity (S m^{-1}) and electric potential (V), respectively.

2.2.3 Mass and momentum transport model

Mass transport ($N_i, mol\ m^{-3}\ s^{-1}$) is calculated by the extended Fick's model (Eq. (10)) and momentum transport is calculated by the Navier-Stokes equation (Eq. (11)) [40].

$$N_i = -\frac{1}{RT}\left(\frac{B_0 y_i P}{\mu}\frac{\partial \mathrm{P}}{\partial \mathrm{z}} - D_i^{eff}\frac{\partial (y_i \mathrm{P})}{\partial \mathrm{z}}\right) \quad (i = 1, \dots, n) \quad (10)$$

$$\rho\frac{\partial u}{\partial t} + \rho u \nabla u = -\nabla p + \nabla[\mu\left(\nabla u + (\nabla u)^T\right) - \frac{2}{3}\mu\nabla u\Big] - \frac{\varepsilon\mu u}{k} \quad (11)$$

where B_0 is the permeability (m^2) of the porous electrodes, y_i is the mole fraction of component i, μ is the gas viscosity (N m^{-1} s^{-1}), D_i^{eff} is the overall effective diffusion coefficient (m^2 s^{-1}) of component i, ρ (kg m^{-3}) is the gas density and u (m s^{-1}) is the velocity vector.

2.2.3 Heat transfer model

General heat balance equation is used to calculate the heat transfer process in DC-SOFC as [40]:

$$\rho C_p u \cdot \nabla T + \nabla \cdot \left(-\lambda_{eff} \nabla T\right) = Q \tag{12}$$

where C_p ($J \cdot K^{-1}$) is the heat capacity of fluid, u is the fluid velocity field, λ_{eff} ($W \cdot m^{-1} K^{-1}$) is the effective heat conductivity and Q (J s^{-1}) is the heat source term.

To evaluate the electrical efficiency of DC-SOFC (η_{SOFC}), both electrical power output (P_{SOFC}) and heat (Q) should be considered. η_{SOFC} is defined as

$$\eta_{SOFC} = \frac{P_{SOFC}}{P_{SOFC} + Q} \tag{13}$$

The overall rate of heat rejection Q in the DC-SOFC is positive at a high current density (the value of heat released from DC-SOFC is defined as positive in the present paper). The heat Q in DC-SOFC can be further given by

$$Q = Q_e - Q_c \tag{14}$$

where Q_c (J s^{-1}) is rate of heat absorption by chemical reactions which equals to the enthalpy change of the Boudouard reaction and Q_e (J s^{-1}) includes heat released from the

electrochemical reaction ($-IT\Delta S/2F$, J s^{-1}) and the heat resulted from overpotential losses ($(E-V)I$, J s^{-1}). Thus, Q_e can be calculated as

$$Q_e = -T\Delta S \times \frac{I}{2F} + (E-V)I \tag{15}$$

When $Q_e = Q_c$, i.e., $Q = 0$, one may obtain the thermal neutral current I_{tn} as follows:

$$I_{tn} = \frac{Q_c}{-T\Delta S/2F + E - V} \tag{16}$$

Based on the DC-SOFC model and the relative parameters given in Table 2, one may generate the curves of Q varying with i ($i = I/A$, A is the effective area of DC-SOFC), as shown in Fig. 3. It is seen that Q changes from negative to positive values as the DC-SOFC operating current density increases. When $i < i_{tn}$, i.e., $Q < 0$, the heat produced by the irreversible losses is less than the heat required for the Boudouard reaction. An amount of heat $|Q|$ should be provided from the external heat source to the DC-SOFC to ensure the normal operation, and the left external heat source in Fig. 1 should be switched on. When $i = i_{tn}$, i.e., $Q = 0$, the heat generated due to irreversible losses is equal to the required heat for Boudouard reaction. The DC-SOFC is thermally self-sustained without absorbing or releasing any heat. Therefore, both the left external heat source and the right Stirling cycle in Fig. 1 are unnecessary. When $i > i_{tn}$, i.e., $Q > 0$, the heat generated due to the irreversible losses exceeds the required heat for the Boudouard reaction. The Stirling cycle in Fig. 1 should be switched on, and an amount of heat Q is transferred to the Stirling cycle to produce power P_{SHE}. It can be also found from Fig. 3 that i_{tn} is larger at a higher operating temperature. Thus, more heat can be generated for the endothermic Boudouard reaction. In addition, less heat is generated for the given current density at higher operating temperature as the faster Boudouard reaction at

higher temperature consumes more heat from DC-SOFC.

2.2 Stirling cycle

Stirling cycle consists of four processes including two isothermal processes and two isochoric processes. Considering the finite-rate heat transfer and regenerative losses in the cycle, the performance of the Stirling cycle can be evaluated based on the non-equilibrium thermodynamics. For a given amount of heat Q, the maximum efficiency and the corresponding power output of the Stirling cycle are, respectively, given by [44]

$$\eta_{SHE} = \frac{Q/K + (a-1)T - aT_0 + d}{2aT + a\left[Q/K + (a-1)T - aT_0 + d\right]} \tag{17}$$

and

$$P_{SHE} = Q \times \eta_{SHE} = Q \times \frac{Q/K + (a-1)T - aT_0 + d}{2aT + a\left[Q/K + (a-1)T - aT_0 + d\right]} \tag{18}$$

where $a = xC/[R\ln(V_2/V_1)]$, $d = \sqrt{\left[(a+1)T + aT_0 - Q/K\right]^2 - 4a(a+1)TT_0}$, $K = k_1 \Big/ [(1+b)\left(1+\sqrt{k_1/k_2}\right)^2]$ (J s^{-1} K^{-1}), x is the fractional deviation from ideal regeneration, C is the molar heat capacity (J mol^{-1} K^{-1}) of the working substance in the regenerative processes, V_1 and V_2 are the volume (m^3) of the working substance along the constant-volume heating and cooling processes, k_1 and k_2 are the thermal conductance (J s^{-1} K^{-1}) between the Stirling cycle and the DC-SOFC and the environment, b is the heat-transfer time ratio between the regenerative processes and the isothermal processes. The parameters of the Stirling cycle can be found in Table 3. For comparison, the power density of the Stirling cycle is given based on the same surface area (A) of DC-SOFC.

2.3 The regenerator

The regenerator in Fig. 1 functions as a counter-flow heat exchanger that continuously preheats the inlet activated carbon and air using the heat contained in the outlet products. The products are cooled down to the environmental temperature and the solid carbon and oxygen are heated to the operating temperature of the SOFC. According to the parameters given in Table 4, one can prove that

$$\Delta Q_{CO} - \left(\Delta Q_C + \Delta Q1_{O_2}\right) > 0 \tag{19}$$

$$\Delta Q_{CO_2} - \left(\Delta Q_C + \Delta Q2_{O_2}\right) > 0 \tag{20}$$

where $\Delta Q_{CO} = \dot{m}\int_{T_0}^{T} C_{CO} d\tau$, $\Delta Q_C = \dot{m}\int_{T_0}^{T} C_C d\tau$, $\Delta Q1_{O_2} = 0.5\dot{m}\int_{T_0}^{T} C_{O_2} d\tau$, $\Delta Q2_{O_2} = \dot{m}\int_{T_0}^{T} C_{O_2} d\tau$, $\Delta Q_{CO_2} = \dot{m}\int_{T_0}^{T} C_{CO_2} d\tau$, $\dot{m}$ is the molar consumption rate of solid carbon, T_0 is the ambient temperature (K), C_j is the isobaric molar heat capacities (J mol^{-1} K^{-1}) for species j (j = solid carbon, CO, O_2 or CO_2). As there is only CO or CO_2 in the anode outlet gas, it can be concluded that the heat contained in the products is always enough to preheat the reactants to attain the operating temperature of the DC-SOFC regardless of the molar fraction of CO and CO_2 (the inlet N_2 in air is supposed to be preheated by the outlet N_2). Since some high-effectiveness regenerators have already been reported [45], it is proper to assume that the regenerator in Fig. 1 performs perfect regeneration.

2.4 The performance of the hybrid system

As the waste heat from DC-SOFC is used to preheat the solid carbon and air at the inlet of the cell, the heat loss from the DC-SOFC system to the environment is negligible against the electrical power P_{SOFC} . Adding the contribution of the Stirling cycle, the overall power output

P and equivalent efficiency η of the hybrid system can be, respectively, expressed as:

$$P=\begin{cases}=P_{SOFC} & \left(i<i_{tn}\right)\\ =P_{SOFC}+P_{SHE} & \left(i\geq i_{tn}\right)\end{cases} \tag{21}$$

and

$$\eta=\begin{cases}=\dfrac{P_{SOFC}}{P_{SOFC}+\left|Q\right|} & \left(i<i_{tn}\right)\\ =\dfrac{P_{SOFC}+P_{SHE}}{P_{SOFC}+Q} & \left(i\geq i_{tn}\right)\end{cases} \tag{22}$$

3. Results and discussion

According to the above mathematical models and parameters given in Tables 1-3, the performance characteristics of the hybrid system can be analyzed. The parameters are taken as default ones unless specified elsewhere.

3.1 Performance characteristics of the Stirling cycle

As the size of the Stirling cycle engine is often different from that of the DC-SOFC, one may define the equivalent power density of the Stirling cycle as $P_{SHE}^{*}=P_{SHE}/A$. Fig. 4 clearly demonstrates the performance characteristics of the Stirling cycle. The Stirling cycle within the hybrid system can only work in the region of $i>i_{tn}$. It is found that the equivalent power density of the Stirling cycle decreases but the efficiency increases with increasing temperature of the DC-SOFC.

As seen from Fig. 4(a), the equivalent power density of the Stirling cycle engine increases with the increasing operating current density since more heat is generated at a larger operating current density. In addition, more heat is generated at a given current density at a lower

temperature because less heat is required by the boudouard reaction at a lower temperature. Those increased heat leads to the higher power generation from the Stirling cycle. When the DC-SOFC works at a current density of 30000 A m^{-2}, the equivalent power density of the Stirling cycle approximately increases from 3900 W m^{-2} at 1173 K to 4600 W m^{-2} at 1073 K. Different from the power density characteristic of Stirling cycle, its equivalent efficiency is only related to the operating temperature of DC-SOFC. Although the available heat Q decreases at an elevated operating temperature T, a higher operating temperature improves the heat-to-power efficiency. As a result, a higher operating temperature positively improves the Stirling cycle performance, and the effect of the operating temperature on the performance of the Stirling cycle becomes more significant as the operating current density increases.

3.2 Power density improvement in hybrid system

Fig. 5 shows the equivalent power densities of the DC-SOFC, Stirling cycle and hybrid system at different operating temperatures, where $P_{SOFC}^{*} = P_{SOFC} / A$ and $P^{*} = P / A$ are the power densities for the DC-SOFC and the hybrid system, respectively. When $i \le i_{tn}$, the curves of $P^{*} \sim i$ and $P_{SOFC}^{*} \sim i$ are overlapped because the Stirling cycle is not involved in electrical power production. When $i > i_{tn}$, the power density of the Stirling cycle keeps growing as more heat is generated at a higher current density. While for the DC-SOFC, its power density first increases rapidly and then decreases slowly with the increasing operating current density. As a result, the Stirling cycle offers more power density than the DC-SOFC at a relative high operating current density. Due to the monotonically increasing power density of Stirling cycle, the power density of the hybrid system keeps increasing with the rising of current density.

The elevated operating temperature not only improves the performance of the DC-SOFC by promoting its electrochemical reactivity, ionic conductivity and gas effective diffusion but also enhances the power output and efficiency of the Stirling cycle. Therefore, a higher operating temperature is favored for the hybrid system to obtain a higher output power density.

3.3 Efficiency characteristics of hybrid system

Fig. 6 shows the equivalent efficiencies of the DC-SOFC, Stirling cycle and hybrid system under different operating temperature. Similarly, the curves of $\eta \sim i$ and $\eta_{SOFC} \sim i$ are overlapped in the region of $i \le i_{tn}$. The efficiency of the DC-SOFC is quite high at a small operating current density and reaches 100% when the DC-SOFC is working at a current density of i_{tn}. The efficiency of the DC-SOFC rapidly decreases with a further increase in operating current density. With the help of Stirling cycle, more than 30% improvement of efficiency can be achieved. Due to the higher efficiency of Stirling cycle at higher operating temperature, the efficiency improvement is more significant at higher operating temperatures.

3.4 Effect of distance between carbon layer and anode electrode

In DC-SOFCs, the distance between carbon layer and anode will increase with the consumption of solid carbon. Thus, the transport of CO from carbon layer to anode could be a limiting factor for its power output and has great effect on the heat generation.

The effects of distance between carbon layer and anode electrode on the performance of the hybrid system are shown in Fig. 7. When the distance decreases from 559 μm to 59 μm, a significant performance improvement of the hybrid system is found with the peak power density increasing from 6000 W m^{-2} to 10000 W m^{-2}. As analyzed in our previous papers [22,

23], a smaller distance between carbon layer and anode helps to maintain a higher fuel concentration in the anode, which results in a higher power density of DC-SOFCs. Meanwhile, more heat is generated in DC-SOFCs at a higher electrochemical reaction rate mainly due to the increased entropy change. Thus, more power can be generated from the bottoming Stirling cycle. As a result, both the equivalent power density and efficiency of the hybrid system increase with decreasing distance and this effect becomes more pronounced at a larger current density.

4. Conclusions

The previously developed 2D tubular DC-SOFC model shows that the overall heat generated in the cell could be smaller than, equal to or higher than the heat required by the internal Boudouard reaction. An external heat source and a Stirling cycle are proposed to deal with the heat management problem of the DC-SOFC. Three operation modes are presented based on the different operating conditions. The analytical expressions for the DC-SOFC system under different operating conditions are derived to evaluate its performance. The results show that the proposed system is technically feasible and effective, and the equivalent power density and efficiency of the proposed system could be increased by 4000 W m^{-2} and 30%, respectively. Parametric studies show that the increase of operating temperature would decrease the amount of waste heat and more power would be delivered from the Stirling cycle. Consequently, a higher operating temperature would increase the overall power density and efficiency of the DC-SOFC system. Furthermore, both the equivalent power density and

efficiency of the DC-SOFC system are increased with decreasing distance between carbon layer and anode electrode. The results obtained in this work may provide some theoretical bases for the heat management of a real DC-SOFC.

Acknowledgement

This research is supported by the Natural Science Foundation of Zhejiang Province (Grant No. LQ14E060001), National Natural Science Foundation of China (Grant No. 51406091), Guangdong Innovative and Entrepreneurial Research Team Program (No. 2014ZT05N200), a grant (PolyU 152127/14E) from Research Grant Council, University Grants Committee, Hong Kong SAR, and a grant from Environment and Conservation Fund (ECF 54/2015), Hong Kong SAR.

Nomenclature

Abbreviation

CHP	Combined heat and power
DC-SOFC	Direct-carbon solid oxide fuel cell
LSM	Strontium-doped lanthanum manganite
SCCM	Standard cubic centime per minute
SHE	Stirling cycle
SOFC	Solid oxide fuel cell
TPB	Triple phase boundary
YSZ	Yttrium stabilized zirconium

Roman

a	Constant in Eqs. (6) and (7)
b	Heat-transfer time ratio
B_0	Permeability coefficient, m^2
c_{CO_2}	Molar concentration of carbon dioxide, $mol \cdot m^{-3}$
C	Mole heat capacity of the working substance, J mol^{-1} K^{-1}
C_j	Isobaric molar heat capacities for species j, J mol^{-1} K^{-1}
d	Temperature-dependent parameter in Eqs. (6) and (7), K
D_i^{eff}	Effective diffusivity of species i, $m^2 \cdot s^{-1}$
D_{ik}^{eff}	Knudsen diffusion coefficient of i, $m^2 \cdot s^{-1}$
D_{im}^{eff}	Molecular diffusion coefficient of i, $m^2 \cdot s^{-1}$
E	Output voltage, V
E_{acv}	Activation energy, $J \cdot mol^{-1}$
E_{CO}	Equilibrium potential for carbon monoxide oxidization, V

E_{CO}^{0}	Standard equilibrium potential for carbon monoxide oxidization, V
E_{eq}	Equilibrium Nernst potential, V
F	Faraday constant, 96485 C·mol^{-1}
i_o	Exchange current density, A·m^{-2}
k	Thermal conductance, J s^{-1} K^{-1}
$\dot{m}$	Molar consumption rate of solid carbon, mol· s^{-1}
n	Number of electrons transferred per electrochemical reaction
N_i	Flux of mass transport, kg·m^{-3}·s^{-1}
P	Power density, W m^{-2}
p	(partial) Pressure, Pa
Q	Heat, J s^{-1}
R	Gas constant, 8.314 J·mol^{-1}·K^{-1}
R_{ce}	Reaction rate of Boudouard reaction, mol·m^{-3}·s^{-1}
T	Temperature, K
u	Velocity field, m^{3}·s^{-1}
V	Output voltage, V
V_1, V_2	Volume of the working substance along the constant-volume heating and cooling processes, m^{3}
x	Fractional deviation from ideal regeneration
y_i	Molar fraction of component i

Greek letters

α	Charge transfer coefficient
β_{H_2}	Electrochemical kinetics parameter for H_2
ε	Porosity
η	Efficiency
η_{act}	Activation polarization, V

η_{ohmic}	Ohmic polarization, V
κ	Permeability, m^2
λ	Thermal conductivity, $W \cdot m^{-1}K^{-1}$
μ	Dynamic viscosity of fluid, Pa·s
ρ	Fluid density, $kg \cdot m^{-3}$
σ	Conductivity, S/m
τ	Tortuosity
∅	Potential, V

Subscripts

an	Anode
ca	Cathode
co	Carbon monoxide
f	fraction
H_2	Hydrogen
l	Ionic phase
s	Electronic phase

Superscripts

0	Parameter at equilibrium conditions
eff	Effective
L	Local

References

[1] Cao T, Huang K, Shi Y, Cai N. Recent advances in high-temperature carbon-air fuel cells. Energy & Environmental Science. 2017;10:460-90.
[2] Gür TM. Comprehensive review of methane conversion in solid oxide fuel cells: Prospects for efficient electricity generation from natural gas. Progress in Energy and Combustion Science. 2016;54:1-64.
[3] Jiang C, Ma J, Corre G, Jain SL, Irvine JTS. Challenges in developing direct carbon fuel cells. Chemical Society Reviews. 2017;46:2889-912.
[4] Gür TM. Critical Review of Carbon Conversion in "Carbon Fuel Cells". Chemical Reviews. 2013;113:6179-206.
[5] Hao W, Mi Y. Evaluation of waste paper as a source of carbon fuel for hybrid direct carbon fuel cells. Energy. 2016;107:122-30.
[6] Zhang H, Chen L, Zhang J, Chen J. Performance analysis of a direct carbon fuel cell with molten carbonate electrolyte. Energy. 2014;68:292-300.
[7] Wang H, Cao T, Shi Y, Cai N, Yuan W. Liquid antimony anode direct carbon fuel cell fueled with mass-produced de-ash coal. Energy. 2014;75:555-9.
[8] Jiang C, Ma J, Bonaccorso AD, Irvine JTS. Demonstration of high power, direct conversion of waste-derived carbon in a hybrid direct carbon fuel cell. Energy & Environmental Science. 2012;5:6973-80.
[9] Giddey S, Badwal SPS, Kulkarni A, Munnings C. A comprehensive review of direct carbon fuel cell technology. Progress in Energy and Combustion Science. 2012;38:360-99.
[10] Ni M, Leung MKH, Leung DYC. Technological development of hydrogen production by solid oxide electrolyzer cell (SOEC). International Journal of Hydrogen Energy. 2008;33:2337-54.
[11] Ni M, Leung DYC, Leung MKH. Electrochemical modeling and parametric study of methane fed solid oxide fuel cells. Energy Conversion and Management. 2009;50:268-78.
[12] Nakagawa N, Ishida M. Performance of an internal direct-oxidation carbon fuel cell and its evaluation by graphic exergy analysis. Industrial & Engineering Chemistry Research. 1988;27:1181-5.
[13] Lee AC, Mitchell RE, Gür TM. Thermodynamic analysis of gasification-driven direct carbon fuel cells. Journal of Power Sources. 2009;194:774-85.
[14] Gür TM, Huggins RA. Direct Electrochemical Conversion of Carbon to Electrical Energy in a High Temperature Fuel Cell. Journal of The Electrochemical Society. 1992;139:L95-L7.
[15] Li C, Shi Y, Cai N. Mechanism for carbon direct electrochemical reactions in a solid oxide electrolyte direct carbon fuel cell. Journal of Power Sources. 2011;196:754-63.
[16] Xie Y, Tang Y, Liu J. A verification of the reaction mechanism of direct carbon solid oxide fuel cells. Journal of Solid State Electrochemistry. 2012;17:121-7.

[17] Cai W, Liu J, Xie Y, Xiao J, Liu M. An investigation on the kinetics of direct carbon solid oxide fuel cells. Journal of Solid State Electrochemistry. 2016;20:2207-16.
[18] Wu Y, Su C, Zhang C, Ran R, Shao Z. A new carbon fuel cell with high power output by integrating with in situ catalytic reverse Boudouard reaction. Electrochemistry Communications. 2009;11:1265-8.
[19] Li C, Shi Y, Cai N. Performance improvement of direct carbon fuel cell by introducing catalytic gasification process. Journal of Power Sources. 2010;195:4660-6.
[20] Tang Y, Liu J. Effect of anode and Boudouard reaction catalysts on the performance of direct carbon solid oxide fuel cells. International Journal of Hydrogen Energy. 2010;35:11188-93.
[21] Xie Y, Cai W, Xiao J, Tang Y, Liu J, Liu M. Electrochemical gas-electricity cogeneration through direct carbon solid oxide fuel cells. Journal of Power Sources. 2015;277:1-8.
[22] Xu H, Chen B, Zhang H, Kong W, Liang B, Ni M. The thermal effect in direct carbon solid oxide fuel cells. Applied Thermal Engineering. 2017;118:652-62.
[23] Xu H, Chen B, Liu J, Ni M. Modeling of direct carbon solid oxide fuel cell for CO and electricity cogeneration. Applied Energy. 2016;178:353-62.
[24] Eveloy V, Karunkeyoon W, Rodgers P, Al Alili A. Energy, exergy and economic analysis of an integrated solid oxide fuel cell – gas turbine – organic Rankine power generation system. International Journal of Hydrogen Energy. 2016;41:13843-58.
[25] Pirkandi J, Mahmoodi M, Ommian M. Thermo-economic performance analysis of a gas turbine generator equipped with a pressurized and an atmospheric solid oxide fuel cell. Energy Conversion and Management. 2017;136:249-61.
[26] Khani L, Mahmoudi SMS, Chitsaz A, Rosen MA. Energy and exergoeconomic evaluation of a new power/cooling cogeneration system based on a solid oxide fuel cell. Energy. 2016;94:64-77.
[27] Sharma M, N R, Dasappa S. Solid oxide fuel cell operating with biomass derived producer gas: Status and challenges. Renewable and Sustainable Energy Reviews. 2016;60:450-63.
[28] Zhang X, Ni M, Dong F, He W, Chen B, Xu H. Thermodynamic analysis and performance optimization of solid oxide fuel cell and refrigerator hybrid system based on H2 and CO. Applied Thermal Engineering. 2016;108:347-52.
[29] Hering M, Brouwer J, Winkler W. Dynamic model of a micro-tubular solid oxide fuel cell stack including an integrated cooling system. Journal of Power Sources. 2017;342:504-14.
[30] Adam A, Fraga ES, Brett DJL. Options for residential building services design using fuel cell based micro-CHP and the potential for heat integration. Applied Energy. 2015;138:685-94.
[31] Masoud R. Thermodynamic analyses of municipal solid waste gasification plant integrated with solid oxide fuel cell and Stirling hybrid system. International Journal of Hydrogen Energy. 2015;40:7855-69.
[32] Leonardo P, Masoud R. Thermodynamic Analysis of an Integrated Gasification Solid

Oxide Fuel Cell Plant with a Kalina Cycle. International Journal of Green Energy. 2015;12:610-9.
[33] Kang S, Ahn K-Y. Dynamic modeling of solid oxide fuel cell and engine hybrid system for distributed power generation. Applied Energy. 2017;195:1086-99.
[34] Eveloy V, Rodgers P, Al Alili A. Multi-objective optimization of a pressurized solid oxide fuel cell – gas turbine hybrid system integrated with seawater reverse osmosis. Energy. 2017;123:594-614.
[35] Buonomano A, Calise F, d'Accadia MD, Palombo A, Vicidomini M. Hybrid solid oxide fuel cells–gas turbine systems for combined heat and power: A review. Applied Energy. 2015;156:32-85.
[36] Zhang H, Xu H, Chen B, Dong F, Ni M. Two-stage thermoelectric generators for waste heat recovery from solid oxide fuel cells. Energy. 2017;132:280-8.
[37] Ahmadi MH, Ahmadi MA, Pourfayaz F, Bidi M, Hosseinzade H, Feidt M. Optimization of powered Stirling heat engine with finite speed thermodynamics. Energy Conversion and Management. 2016;108:96-105.
[38] Liao T, Lin J. Optimum performance characteristics of a solar-driven Stirling heat engine system. Energy Conversion and Management. 2015;97:20-5.
[39] Ahmadi MH, Sayyaadi H, Dehghani S, Hosseinzade H. Designing a solar powered Stirling heat engine based on multiple criteria: Maximized thermal efficiency and power. Energy Conversion and Management. 2013;75:282-91.
[40] Ahmadi MH, Sorouri Ghare Aghaj S, Nazeri A. Prediction of power in solar stirling heat engine by using neural network based on hybrid genetic algorithm and particle swarm optimization. Neural Computing and Applications. 2013;22:1141-50.
[41] Rokni M. Thermodynamic analysis of SOFC (solid oxide fuel cell)–Stirling hybrid plants using alternative fuels. Energy. 2013;61:87-97.
[42] Rokni M. Biomass gasification integrated with a solid oxide fuel cell and Stirling engine. Energy. 2014;77:6-18.
[43] Rokni M. Thermodynamic and thermoeconomic analysis of a system with biomass gasification, solid oxide fuel cell (SOFC) and Stirling engine. Energy. 2014;76:19-31.
[44] Chen J, Yan Z, Chen L, Andresen B. Efficiency bound of a solar-driven stirling heat engine system. Int J Energ Res. 1998;22:805-12.
[45] Sadrameli SM. Mathematical models for the simulation of thermal regenerators: A state-of-the-art review. Renewable and Sustainable Energy Reviews. 2016;58:462-76.
[46] Eguchi K, Setoguchi T, Inoue T, Arai H. Electrical-Properties of Ceria-Based Oxides and Their Application to Solid Oxide Fuel-Cells. Solid State Ionics. 1992;52:165-72.
[47] Luo Y, Shi Y, Li W, Cai N. Comprehensive modeling of tubular solid oxide electrolysis cell for co-electrolysis of steam and carbon dioxide. Energy. 2014;70:420-34.
[48] Yaqi L, Yaling H, Weiwei W. Optimization of solar-powered Stirling heat engine with finite-time thermodynamics. Renewable Energy. 2011;36:421-7.
[49] Todd B, Young JB. Thermodynamic and transport properties of gases for use in solid oxide fuel cell modelling. Journal of Power Sources. 2002;110:186-200.
[50] Ho FH. Graphite design handbook. ; General Atomics, San Diego, CA (US); 1988. p.

Medium: P; Size: 122 p. pages.

List of Tables

Table 1. Parameters used in DC-SOFC model [23, 46, 47]

Parameters	Value or expression	Unit
Ionic conductivity		
GDC	$\frac{100}{T} \times 10^{(6.66071\ -\ \frac{5322.92}{T})}$	S m^{-1}
YSZ	$3.34 \times 10^4 e^{\frac{-10300}{T}}$	S m^{-1}
Electronic conductivity		
Ag	$\frac{1.59e^8}{(0.0038T-0.1134)}$	S m^{-1}
Porosity		
Cathode	0.46	
Anode	0.46	
Electrode volume fraction		
GDC	0.21	
Ag	0.79	
S_{TPB}		
Cathode layer	2.14×10^5	$m^2\ m^{-3}$
Anode layer	2.14×10^5	$m^2\ m^{-3}$
Tortuosity		
Cathode	3	
Anode	3	
Exchange current density		
CO	450	A m^{-2}
O_2	400	A m^{-2}
Charge transfer coefficient		
CO	0.5	
O_2	0.5	
Equilibrium constant of Boudouard reaction	6×10^{13}	s^{-1}
Activation energy of Boudouard reaction	$E_{rb} = 248$	$kJ\ \ mol^{-1}$

Table 2. Parameters used in Stirling cycle [39, 48]

Parameter	Value
Mole heat capacity of the working substance C (J mol^{-1} K^{-1})	15
Working substance volume ratio, V_2/V_1	2
Thermal conductance, k_1 (W K^{-1})	200
Thermal conductance, k_2 (W K^{-1})	200
Fractional deviation from ideal regeneration, x	20%
Heat-transfer time ratio, b	1
Environment temperature, T_0 (K)	298

Table 3. Isobaric molar heat capacities for the involved species[49, 50]

Species	Isobaric molar heat capacity $C_{p,l}$(J/mol K)
CO_2	$4.3669+0.2046T-4.7133\times10^{-4}T^2+6.5788\times10^{-7}T^3$ $-5.199\times10^{-10}T^4+2.1458\times10^{-13}T^5-3.5992\times10^{-17}T^6$
O_2	$34.85-5.7975\times10^{-2}T+2.0368\times10^{-4}T^2-3.0037\times10^{-7}T^3$ $+2.3172\times10^{-10}T^4-9.1821\times10^{-14}T^5+1.4776\times10^{-17}T^6$
CO	$30.429-8.1781\times10^{-3}T-5.2062\times10^{-6}T^2+4.1974\times10^{-8}T^3$ $-6.6346\times10^{-11}T^4+3.7756\times10^{-14}T^5-7.6538\times10^{-18}T^6$
Solid carbon	$27.21876-1.21838\times10^{-4}T-4.5324\times10^{4}T^{-1}$ $-2.1815\times10^{6}T^{-2}+7.99859\times10^{8}T^{-3}-7.21429\times10^{10}T^{-4}$

List of Figures

Fig. 1.

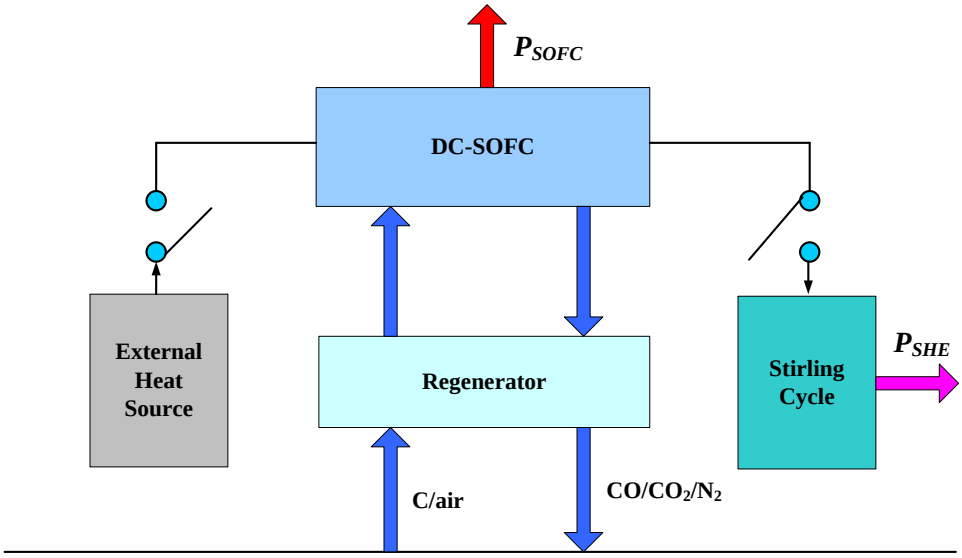

Fig. 1. Schematic diagram of a DC-SOFC based hybrid system.

Fig. 2.

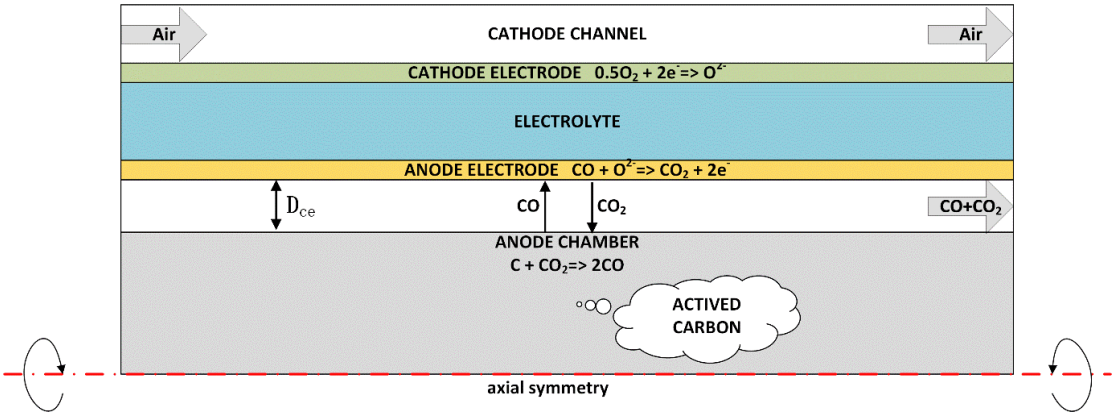

Fig.2. Schematic of electrolyte supported DC-SOFC.

Fig. 3.

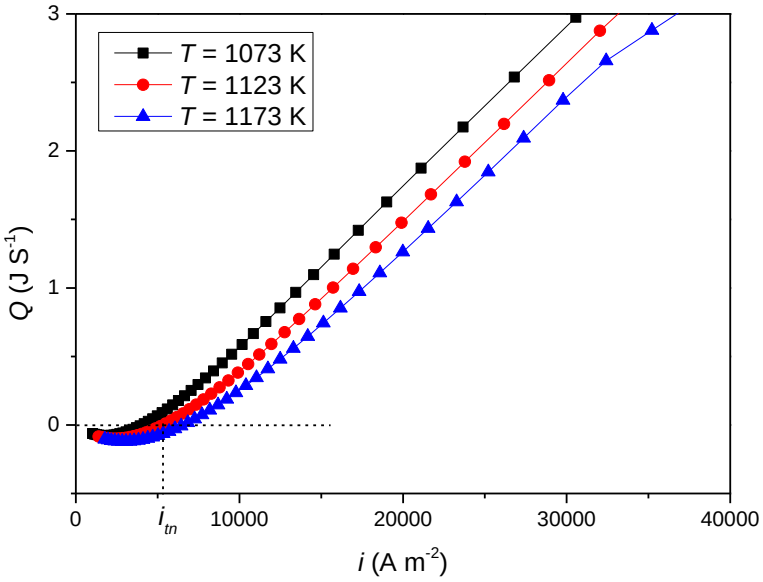

Fig. 3. The curves of Q versus current density under different operating temperature, where $i_{tn} = I_{tn} / A$, A is the polar plate area of the DC-SOFC.

Fig. 4.

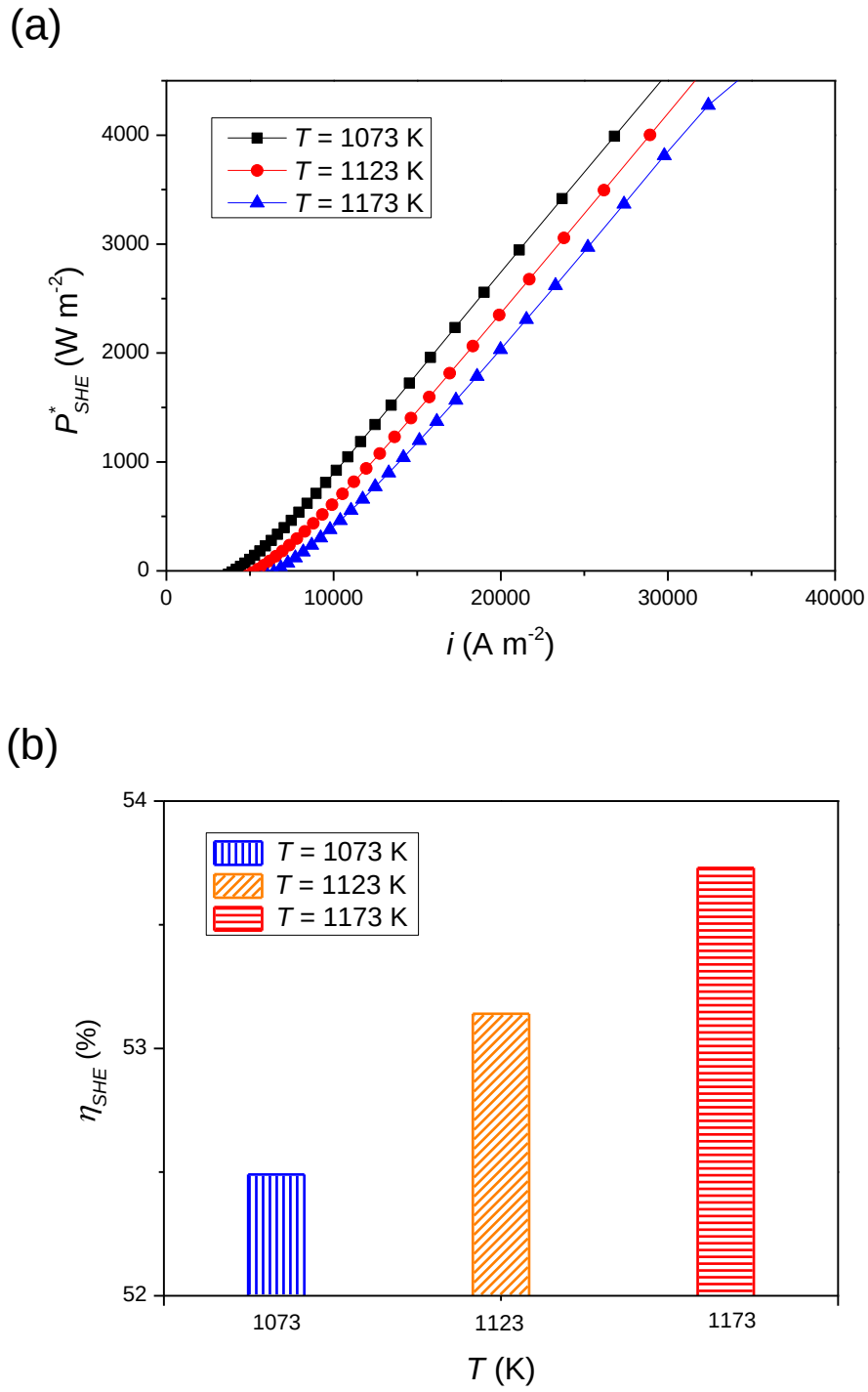

Fig. 4. The (a) equivalent power density, and (b) efficiency of the Stirling cycle under different operating temperature, where $P^*_{SHE} = P_{SHE} / A$ is the equivalent power density of the Stirling cycle.

Fig. 5.

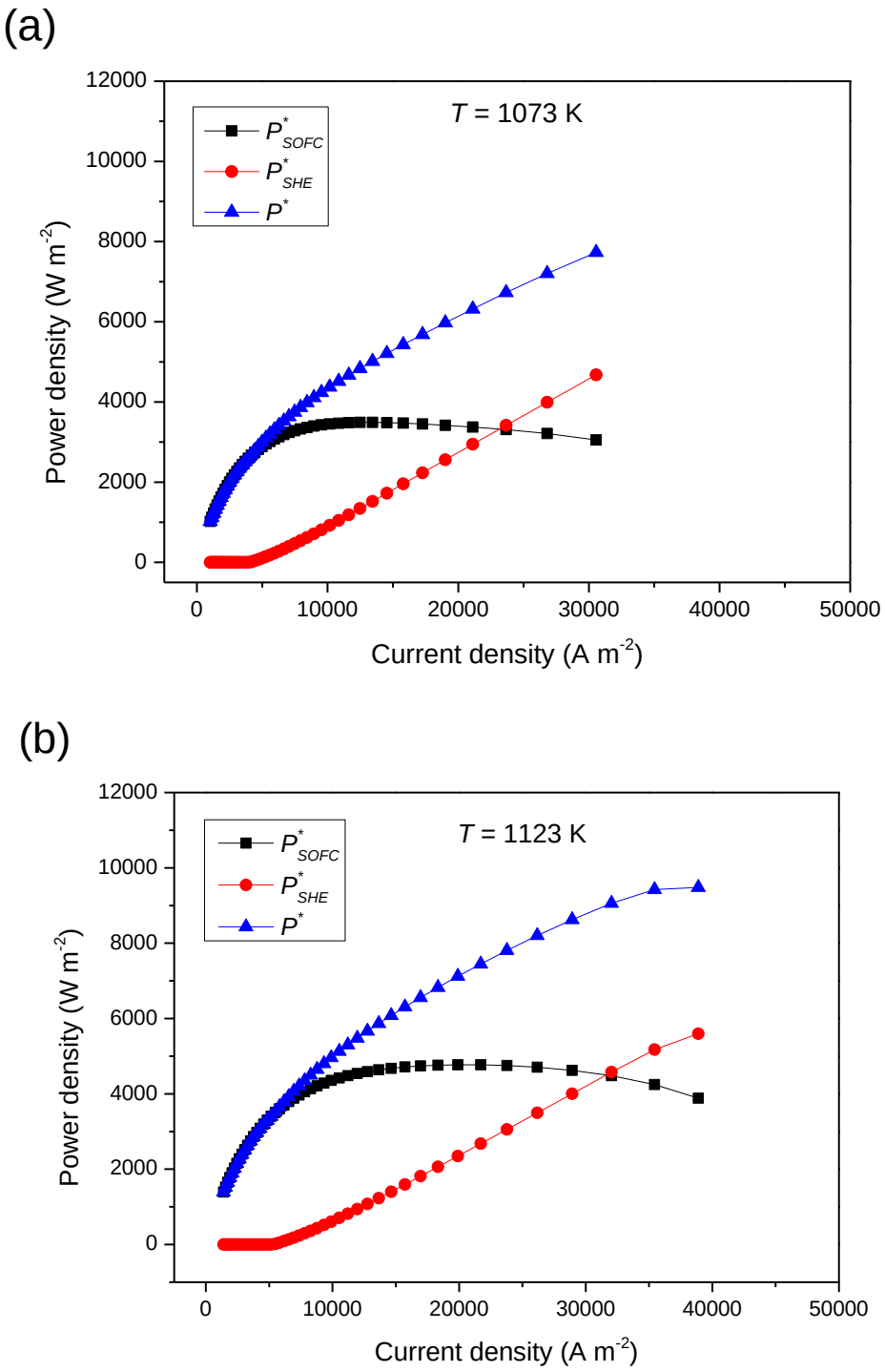
(a)
T = 1073 K
P*SOFC
P*SHE
P*
Power density (W m-2)
Current density (A m-2)
0
2000
4000
6000
8000
10000
12000
0
10000
20000
30000
40000
50000
(b)
T = 1123 K
P*SOFC
P*SHE
P*
Power density (W m-2)
Current density (A m-2)
0
2000
4000
6000
8000
10000
12000
0
10000
20000
30000
40000
50000

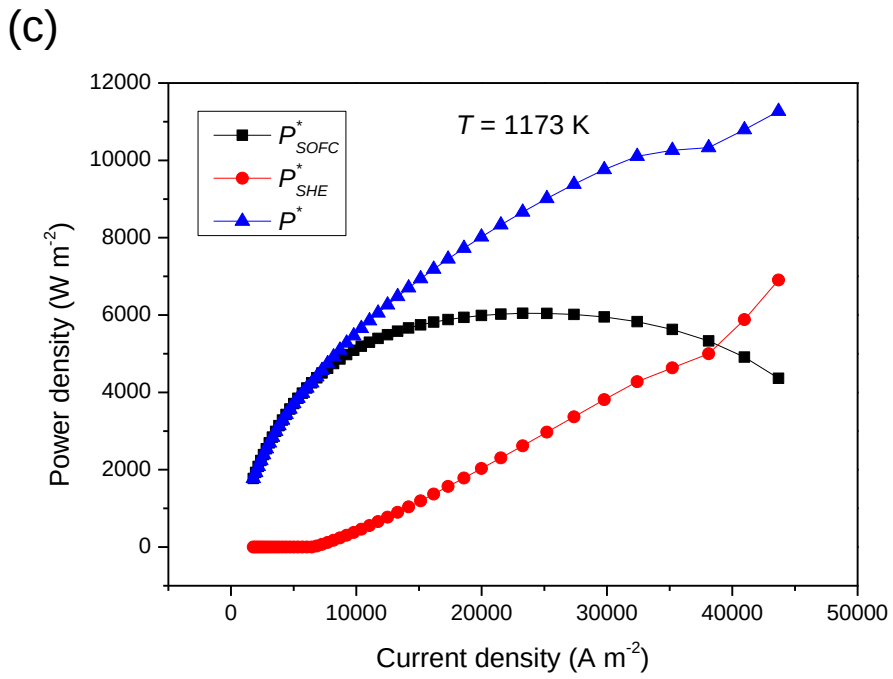

Fig. 5. Equivalent power densities of the DC-SOFC, Stirling cycle and hybrid system at (a) 1073 K, (b) 1123 K and (c) 1173 K.

Fig. 6.

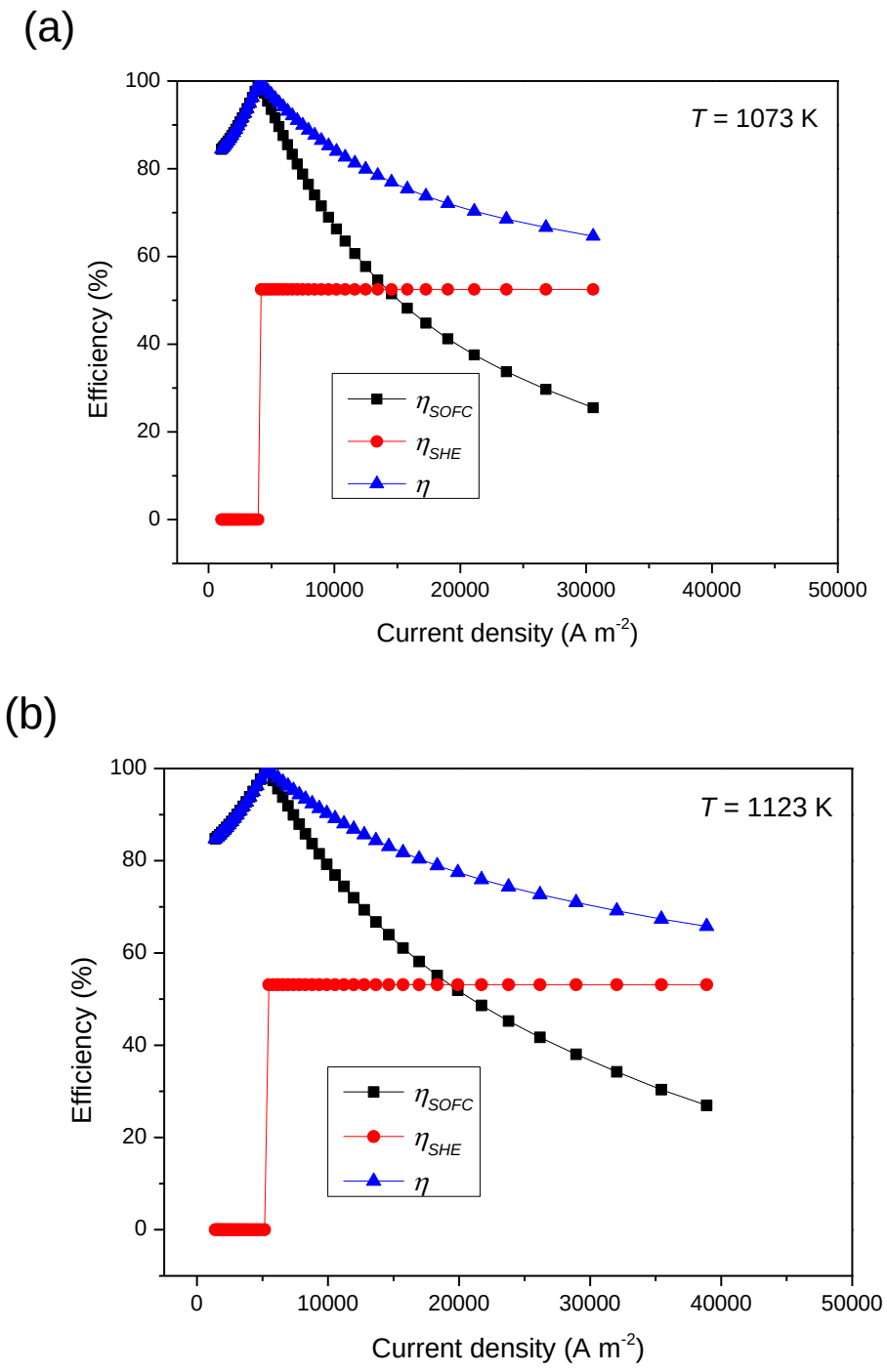
(a)
T = 1073 K
Efficiency (%)
Current density (A m-2)
ηSOFC
ηSHE
η
(b)
T = 1123 K
Efficiency (%)
Current density (A m-2)
ηSOFC
ηSHE
η

(c)

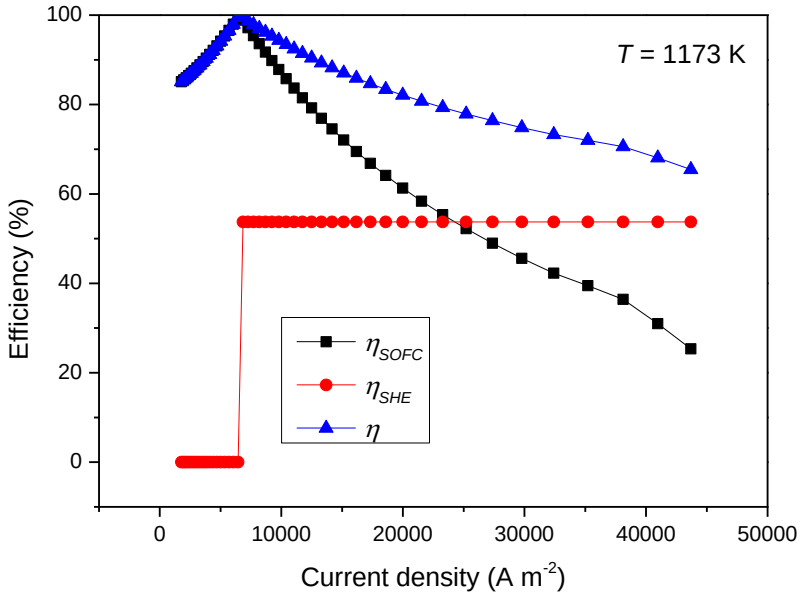

Fig. 6. Equivalent efficiencies of the DC-SOFC, Stirling cycle and hybrid system at (a) 1073 K, (b) 1123 K and (c) 1173 K.

Fig. 7.

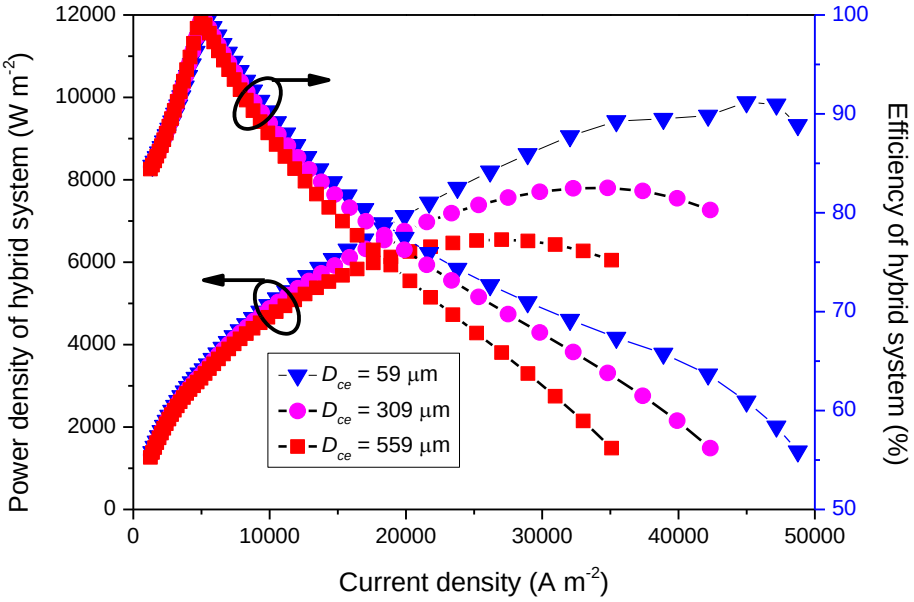

Fig.7. Effects of distance between carbon layer and anode electrode on the performance of the hybrid system.